Variability of white dwarf debris disks

Amelie Bormann

Division of Astrophysics
Department of Physics

LUND
UNIVERSITY

2024–EXA226

Degree project of 15 higher education credits
June 2024

Supervisors: Alexander Mustill & Judith Korth

Division of Astrophysics
Department of Physics
Box 118
SE-221 00 Lund
Sweden

Abstract

Disks around single white dwarfs have been observed as infrared excesses since 1987. Over time, these excesses have shown variability, leading to the conclusion that these debris disks undergo changes. However, the infrared excess should not be the only detectable signature from these disks. They are also expected to reflect visible light, a phenomenon yet to be studied for white dwarf debris disks. This project aims to first find disk parameters that approximately reproduce the observed changes in infrared excess. These parameters will then be used to predict the amount of visible reflected light and asses its detectability. In doing so, I rederive the flat disk model originally proposed by Jura and add one parameter for the albedo and one for the packing fraction of the disk. Next, I derive two models for the reflected light: one assuming a Lambertian surface and one using the Henyey–Greenstein phase function. I find that the flat disk model can match the observed variability when allowing changes in packing fraction. Such changes can for example correspond to mass loss due to collisional grinding within the disk. The reflected light coming from the disk makes up about 0.03% of the stellar light, which could be detectable using relative photometry over months and years using a precise telescope such as CHEOPS, TESS, or PLATO.

Popular summary

Despite the misleading name white dwarfs have nothing to do with Snow White and the Seven Dwarfs from Grimm's fairytales. Instead, these types of stars unfold the final chapter of the fascinating life cycle of a star. When a star runs out of fuel a series of events takes place leading to drastic changes. Planets close to the star are either engulfed by the dying star or destroyed by collisions with other objects. The core of the star, known as a white dwarf, is the only remainder of this destructive event. For many years this was thought to be true until dust was found to orbit a white dwarf by Zuckerman and Becklin in 1987. Since then, more and more white dwarfs have been found to host rings of dust. These so-called debris disks give rise to many questions: How do these rocks survive the violent death of the star? What do these disks look like and what are they made of?

Answering these questions is challenging since one cannot quickly send a spacecraft to a white dwarf and take a picture. Instead, one must measure the incoming light from the star and create theoretical models that can explain the observations. As if this was not difficult enough, these disks seem to change with time, as recent observations show. This variability is yet unexplained, but with the help of more advanced mathematical models, astrophysicists are on the hunt for answers.

The easiest way to imagine the debris around white dwarfs is by viewing them as a similar system to Saturn and its rings: a so-called flat debris disk. Rocks of many different sizes and forms lie in the same plane and orbit around the star. If this disk then becomes smaller or larger in radius, the light measured from the white dwarf is going to look different. Depending on how many rocks there are in the disk, or in other words, how packed the disk is, the observed spectrum changes as well.

In my project, I derive two models for debris disks: one that simulates the light coming from the disk heating up, also called the infrared excess and one that simulates the reflected light from the disk. Each model has parameters that describe different properties of the disks. By changing them, I can see how different disks correspond to different spectra. This knowledge is helpful to for example see what parameters of the infrared excess model I have to change to match the observed variability of the disk. Using these parameters, I can then show what the reflected light is expected to look like in theory. This endeavour is particularly valuable given that reflected light from a white dwarf debris disk has not been observed yet.

White dwarfs are the remains after a star dies, yet their story is still unfolding. A fascinating part of this story are debris disks, which describe the rock formations orbiting these stars. To understand the stories behind white dwarfs and their debris disks one has to look at observed data and establish theoretical models that can recreate the data observed. My models simulate the heat and the reflected light coming from a debris disk and by changing parameters I can see what disk properties correspond to observed spectra.

Contents

Chapter 1

Introduction

White dwarfs are remnants of stars that have come to the end of their lifecycle. After a star has gone through the giant branch phases, all material once orbiting a main–sequence star should have been lost (Veras et al., 2024). But, as observations show, some material survives and is gathered into debris disks. Over the years, various processes leading to the formation and evolution of white dwarf debris disks have been studied in detail. For instance, the material can be delivered to the star through scattering events, where an asteroid approaches close to the star, gets disrupted, and subsequently accreted onto the white dwarf (McDonald and Veras, 2023; Bonsor et al., 2011). The accreted material can then be detected spectroscopically in the white dwarf's atmosphere (Paquette et al., 1986).

The first white dwarf with a dusty disk was found by Zuckerman and Becklin (1987) by observing an excess in radiation in infrared. These observational signatures are known as the infrared excess, which describes a small peak in flux density next to the peak of the white dwarf. These plots are also known as spectral energy distributions (SEDs). Recent observations reveal that these spectral energy distributions vary over time for most white dwarfs with debris disks (Swan et al., 2019, 2020, 2021).

Swan et al. (2019) suggested that this variability arises from the disks changing over different timescales. They observed that the infrared flux variability is common among white dwarf debris disks and that dimming and brightening episodes are equally frequent (Swan et al., 2020). Furthermore, they observed variations in flux over timescales of months to years rather than minutes or hours. The observed infrared variability led to their assumption that collisions most likely drive these flux changes and that dust production is therefore an ongoing process (Swan et al., 2021).

The infrared excess without the variability can be described by the flat disk model originally proposed by Jura (2003). It describes the debris disk as a set of flat and opaque rings around the white dwarf, each with a different temperature. While describing the infrared excess well, a static flat disk model cannot account for the infrared variability observed by Swan et al. (2019).

In this project, I set up models for white dwarfs and their debris disks to study the infrared excess. I start by looking at a simple blackbody, which is followed by the flat disk model by Jura (2003). I then add albedo and packing fraction to the model to examine how

each parameter affects the SED and to see what is needed to match recent observations.

Additionally, I derive two models for reflected light coming from the disk, one simplified model that assumes a Lambertian disk and one model using the Henyey–Greenstein phase function (Henyey and Greenstein, 1941), to study how the infrared variability affects the reflected light. So far, visible light photometry for these white dwarfs has been limited to those where some of the material transits in front of the star. Therefore, using these models, I want to see if the reflected light could be detectable, regardless of the disk orientation.

Chapter 2

Background

2.1 Effects of Stellar Evolution on Planets and Small Bodies

Before a main–sequence (MS) star becomes a white dwarf, it undergoes the giant branch phases. In doing so the star experiences drastic changes, which affect the former planetary system significantly. Three main phenomena occur: mass loss, increase in luminosity, and increase in radius. The star loses a significant fraction of its mass through stellar winds (Prialnik, 2010), which changes the gravitational potential in the system. As a result, the orbits of planetary bodies expand. The luminosity of the star increases by several orders of magnitude and the dust is drawn into the star by *Poynting-Robertson drag* (Bonsor and Wyatt, 2010), while pebbles and asteroids either go inwards or outwards due to the *Yarkovsky effect* (Veras et al., 2015a, 2019). The increase in radius (visualised by the red line in Fig. 2.1) leads to the star engulfing its inner planets. But, since the star is also losing its mass, there is a race between the star and the planetary orbit expanding (Veras et al., 2024). An overview of the effect of stellar evolution on planets is shown in Fig. 2.1.

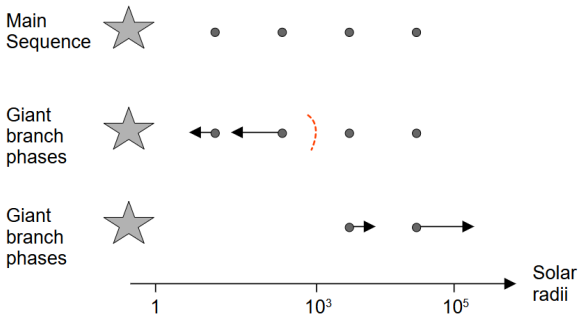

Figure 2.1: The first row shows a planetary system and its host star. As this star goes through the giant branch phases, the planetary system experiences drastic changes. The star engulfs its inner planets due to an increase in radius. Additionally, the star loses mass, leading to the expansion of planetary orbits, as shown in the last row.

After the star has gone through the giant branch phases, dust, and pebbles are redistributed within the system. The remnant core of the star is known as a *white dwarf*. These stars have a small radius but very high surface gravity and their atmospheres should be composed of either hydrogen or helium since any heavier elements are dragged down below the photosphere (Koester, 2009). However, observations show that white dwarf atmospheres can exhibit elements heavier than helium, which leads to the reasoning that these elements must come from accreted material (Paquette et al., 1986).

2.2 Observations

Due to the radius of an MS star expanding drastically during the asymptotic giant branch phases, there should be no material within a few au of the white dwarf. However, there is surprising evidence of material very close to the white dwarf, which can be detected by transits, infrared excess, and emission and absorption lines. A transit can be observed as a decrease in broadband photometric flux followed by an increase. These dimming and brightening events are periodic due to the orbital motion of the material. Therefore, changes in the amount of dimming indicate dynamical activity. A build-up of dust and debris creates many different transit peaks, while sharp dimming events come from planet-like objects (Veras et al., 2024). Transit photometry is only sensitive to planets in close orbit to the white dwarf but such planets are unlikely to survive stellar evolution. This implies that planets on orbits close to white dwarfs should be scarce. However, at least one example is known to host a planet: WD 1856+534. A Jupiter-sized planet was found to orbit this white dwarf by Vanderburg et al. (2020) using NASA's Transiting Exoplanet Survey Satellite (TESS). In the context of debris disks, transit photometry is used to study the evolution of debris around white dwarfs. The debris around ZTF J0139+5245 has a 110-day orbital period. It is assumed to come from a broken-up asteroid initially situated at a distance where tidal forces were insufficient to break it apart (Veras et al., 2020). Another white dwarf, ZTF J0328-1219, exhibits transiting planetary debris with two specific periodicities, which indicate two clumps of debris orbiting the star (Vanderbosch et al., 2021). In conclusion, studying transits can give insights into structures in the disks or evidence for passages of asteroids delivering material.

The study of bodies in transit requires a rather precise alignment of the orbital plane with the line of sight. However, when studying non-aligned debris, alternative methods such as analysing the spectral energy distribution[1] (SED) of the star come into play. These plots show two peaks (see Fig. 2.2, left), where the higher peak is for the white dwarf and the lower peak (at a longer wavelength) is known as the *infrared excess*. The first white dwarf observed to exhibit an infrared excess was G 29-38 by Zuckerman and Becklin (1987). By the use of infrared photometry, they observed an excess emission at wavelengths $> 2\mu$m, which led to their assumption that dust grains orbit this star in a disk. Studying the geometry of these disks is challenging since the correlation between the infrared excess and the geometric configuration is degenerate (Veras et al., 2024). Recent observations

[1] usually flux density versus wavelength plots

show that the infrared excess of most white dwarf debris disks varies over time (see Fig. 2.2, right). Swan et al. (2019) proposed that these flux changes are most likely driven by collisions within the dusty disk. Therefore, dust production must be an ongoing process. Additionally, Swan et al. (2020) observed that the flux changes happen within timescales of months to years rather than minutes to hours and that dimming and brightening events are equally common.

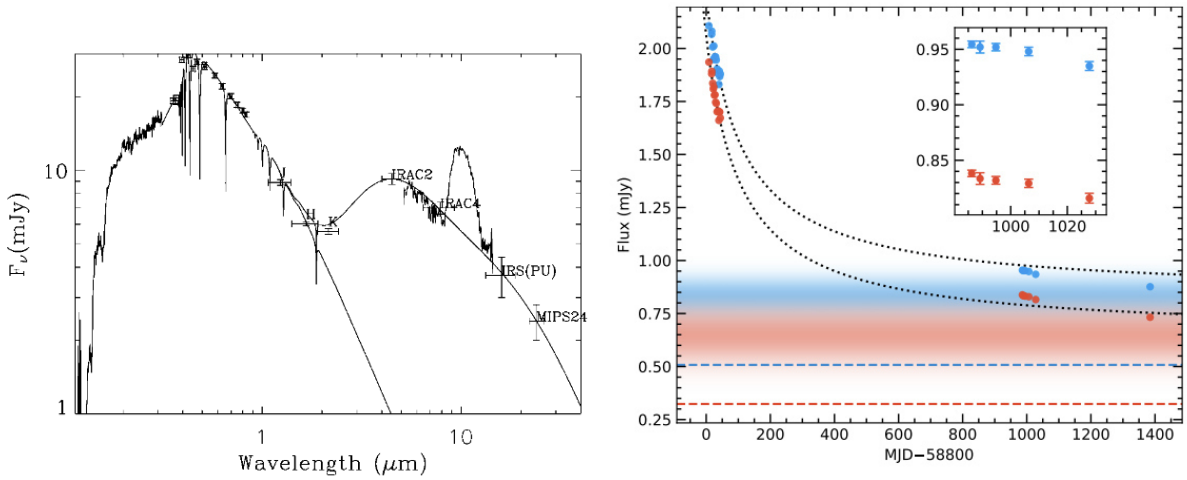

Figure 2.2: *Left:* SED of G 29-38 reprinted from "The Dust Cloud around the White Dwarf G29-38", by Reach et al. (2005). *Right:* Lightcurves of WD 0145+234 taken by *Spitzer* (left of the centre) at 3.6 μm (blue) and 4.5 μm (red) and *JWST* (right of the centre) reprinted from "The first white dwarf debris disk observed by JWST", by Swan et al. (2024). The horizontal lines show the photospheric flux.

The last main type of observations of debris around white dwarfs are emission and absorption lines, which are observed using gas spectroscopy. Emission lines are an indication of gas, which is generated by collisions within the debris disk or sublimation of grains close to the star. They can be used to identify the chemical composition of the gas. Unlike the infrared excess, emission lines can be used to characterise the geometry of the gas using Doppler tomography. The most common polluters for white dwarfs with dusty disks are CaII and Si. It was found that all white dwarfs with CaII emission lines have an infrared excess due to debris disks (Farihi, 2016). Additionally, CaII emission lines are often asymmetric, leading to the conclusion that the gas disk is eccentric. The silicate emission lines, on the other hand, indicate micron-sized dust grains. This dust seems to be carbon-deficient and rocky (Farihi, 2016). Some white dwarfs also exhibit absorption features additional to emission lines. Like emission lines, absorption features for white dwarfs can have asymmetric line profiles and Doppler shifts. WD 1124-293 is an example of a white dwarf that exhibits Ca absorption and photospheric absorption features due to Mg and Fe (Steele et al., 2021).

So far, white dwarfs with gas emissions from the disk exhibit metals in their atmospheres. This could come from an observational bias since detection prefers high abun-

dances of these metals, a strong infrared excess, and strong emission lines from the gas. Emission lines not only indicate the presence of gas but also support the detection of the infrared excess. The gas and dust disks are in the same region around the star, which supports the theories of tidally disrupted bodies forming the disks (Farihi, 2016). Lastly, the emission lines are observed to vary as well (Dennihy et al., 2018). The observed variations are proposed to come from relativistic precession or non-axisymmetric density perturbations within the gas disk.

2.3 Disk Formation and Evolution

Many different processes can deliver material to a white dwarf. The most important concept within this context is the *Roche limit*. It describes a certain region around a star where a body gets tidally disrupted (Lissauer and de Pater, 2013, Chapter 13.1). Outside this region, large bodies, such as asteroids or planets, are held together by self-gravitation. However, when an object reaches the Roche limit, the tidal forces acting on it become larger than its self-gravitation, leading the object to break apart into smaller fragments (see Fig. 2.3, step 2). The Roche limit for white dwarfs is around $0.01R_{\odot}$ to $1R_{\odot}$ (Veras et al., 2024) and the debris disk is usually within 1 $R_{\odot}$ (step 3).

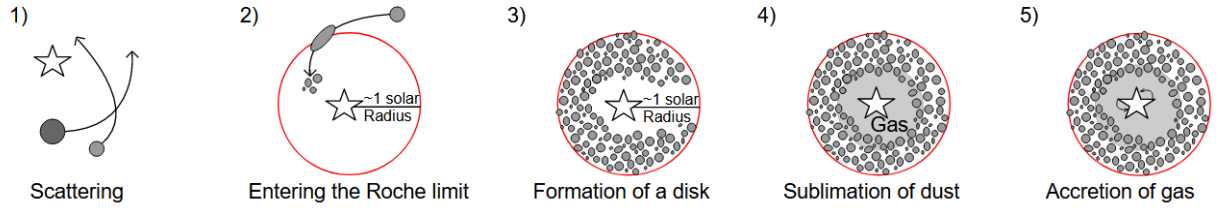

Figure 2.3: One possible delivery mechanism for disks: 1) gravitational interaction between two bodies, 2) as one body reaches the Roche limit, it gets tidally disrupted into smaller fragments, 3) the dust and debris form a disk around the star, 4) the region closest to the star only contains gas due to sublimation of dust, 5) gas is accreted onto the white dwarf.

The mechanism describing the delivery of material to a white dwarf's Roche limit is called pollution (step 1). Pollutants can vary in size from pebbles and dust to planets (Maldonado et al., 2020a,b) or asteroids. Asteroids can be gravitationally perturbed by planets, leading to high orbital eccentricities (McDonald and Veras, 2023; Bonsor et al., 2011). For planets to act as pollutants, they need a giant planet or a companion star to drive the pollution. However, since there are not enough planets per system, planets rarely pollute white dwarfs (Veras et al., 2024). Very small objects, such as pebbles and dust, are common pollutants since a large amount of dust is present after the giant branch phases due to the break-up of asteroids and planets or collisions breaking apart objects. Dust and pebbles are so small that they do not need gravitational interactions from larger bodies to reach the Roche limit. They can sometimes be drawn towards the Roche limit by stellar radiation alone (Veras et al., 2015b; Veras, 2020). Such processes include Poynting-Robertson

drag, which leads centimetre-sized dust grains to spiral inwards, and the Yarkovsky effect, which leads km-sized objects to move inwards or outwards due to irregular temperature distributions on the objects (Lissauer and de Pater, 2013, Chapter 2.8).

If the particles in the disk get too close to the star via radiation effects or collisions, they sublimate. This process creates a gas disk within roughly 1 $R_{\odot}$ around the star (see Fig. 2.3, step 4). The gas is accreted onto the white dwarf (step 5) and in doing so, pollutes its atmosphere in three stages (Farihi, 2016). At first, the metals build up in the outer layers of the white dwarf's atmosphere. In this stage, the ratios of heavy elements in the star and the disk are equal, as the metals have not sunk yet. After that, the system reaches a steady state. Lastly, after the accretion of the gas is completed, the metals remain detectable for many diffusion timescales. This is the time over which these metals diffuse out of the photosphere and sink into the deeper layers of the star. Knowing these timescales helps understand the accretion rates and the timeline of these processes. Detectable metals imply that accretion has occurred relatively recently.

2.4 Disk Models

To interpret the observations, it is necessary to understand the important radiative processes for debris disks. When the incoming radiation from the white dwarf reaches the disk, it is either absorbed, scattered, or transmitted, as shown in Fig 2.4. The transmitted radiation passes through the disk without experiencing any changes. Therefore, it is the same as the incident radiation coming from the white dwarf.
The absorbed and re-emitted radiation can be seen as the infrared excess in SEDs. The absorbed radiation heats the disk, which means the re-emitted radiation can be described as thermal radiation. There are many models describing the infrared excess of white dwarfs. One of the simplest is based on modelling the disk as a blackbody. The most common model is the so-called flat disk model by Jura (2003) derived from a disk model for T Tauri stars by Chiang and Goldreich (1997). The disk is modelled as a set of flat and opaque rings, each having a different temperature. A few years later, Jura et al. (2007) derived a disk model, using a warped disk with a temperature gradient to describe the debris around white dwarf GD 362. This model assumes an opaque disk, where the outer region of the disk absorbs all radiation but is optically thin in infrared. Other disk models include for example eccentric disks (Dennihy et al., 2016) or narrow disks with an opening angle (Ballering et al., 2022)
In the simplest models, the reflected radiation from the disk keeps the same spectrum as the incident radiation[2]. The simplest model for a reflecting surface is a Lambertian surface, which reflects all radiation perfectly diffuse (Karttunen et al., 2017). If the reflecting object is not a Lambertian surface, the reflected radiation depends on the incident angle described by a phase function For small particles, one can use the Henyey–Greenstein (HG) phase function, which gives an approximate solution for diffraction effects when waves interact with particles. For forward scattering, the HG phase function resembles functions derived

[2]In principle, the efficiency of scattering depends on wavelength.

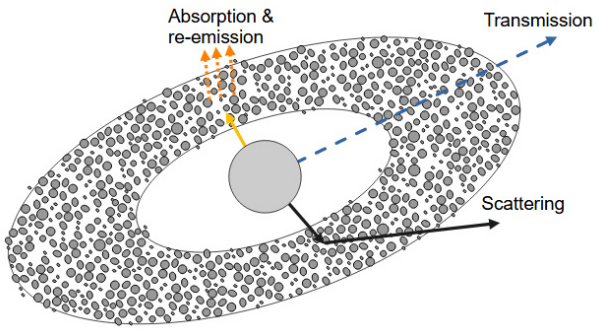

Figure 2.4: Visualization of the radiative processes of the debris disk. The dashed arrow shows transmission of the light through the disk, while the yellow and orange arrows show absorption and re-emission of stellar radiation. The black arrows visualize the scattering of incoming radiation.

based on Mie scattering (Henyey and Greenstein, 1941), where the particles are larger than the wavelength of incident light (Lockwood, 2019). This leads to constructive or destructive interference between the scattered waves (Demtröder, 2017).

So far, studies in visible photometry have only been possible for planets or disks that are passing in front of the white dwarf. The methods of infrared excess and gas spectroscopy are however possible for any disk orientation. My thesis will examine whether one can detect any change in these misaligned disks in optical photometry, which is a gap in current research.

Chapter 3

Method

In this chapter, I implement simple disk models for infrared and reflected visible light. I start by deriving the flux of a white dwarf modelled as a blackbody. This is followed by a simple blackbody model for the disk. Next, I derive the flux of a debris disk according to the flat disk model by Jura (2003). I add albedo and packing fraction as parameters to the flat disk model in §3.1.4 to be able to vary these parameters and see what is needed to roughly match the observed infrared variability. Then, I redo the calculations for reflected visible light in §3.2 starting with a Lambertian surface, which is then followed by a model that uses the Henyey-Greenstein phase function to account for diffraction effects.

3.1 Infrared Excess

3.1.1 Stellar Blackbody Model

To plot the spectral energy distribution of a white dwarf, one has to know the flux density of the star. The spectral flux density, or spectral irradiance, arriving at a detector can be described by (Rutten, 2003, Chapter 2.1)

$$F_\nu = \int I_\nu \cos\theta \; d\Omega \,, \tag{3.1}$$

where I_ν is the specific intensity of the star, $d\Omega$ is the solid angle with polar coordinates θ and ϕ. The star can be assumed to be a point source, such that $\cos\theta = 1$. Additionally, the star is assumed to be a blackbody with a projected emitting area $\Omega = \pi R_*^2/d^2$, where R_* is the radius of the star and d the distance to the detector. The radiation of the star can then be described by the Planck function

$$B_\nu(T_*) = \frac{2h\nu^3}{c^2} \frac{1}{e^{h\nu/k_B T_*} - 1} \,, \tag{3.2}$$

where h is the Planck constant, c is the speed of light, k_B is the Boltzmann constant and ν is the frequency. The flux density is then

$$F_\nu = \frac{\pi}{d^2} B_\nu(T_*) R_*^2 \,, \tag{3.3}$$

with units[1] W m^{-2} Hz^{-1}. To get the flux density in terms of wavelength, one has to note that every frequency interval does not scale the same as every wavelength interval. The Planck function can therefore not simply be rewritten with $c = \lambda\,\nu$. The relation between both Planck functions is $B_\nu\,d\nu = B_\lambda\,d\lambda$ instead. Using $d\nu = -c/\lambda^2\,d\lambda$, the Planck function in wavelength is described by

$$B_\lambda(T_*) = \frac{2hc^2}{\lambda^5}\frac{1}{e^{hc/k_B T_*\lambda} - 1}\,, \tag{3.4}$$

which gives the flux density in wavelength.

3.1.2 Blackbody Disk Model

Similarly to the derivation for the stellar blackbody, one can model the disk as a blackbody by starting with Eq. (3.1). The disk is assumed to be a point source with a projected emitting area of $\Omega = \pi/d^2\cos(i)(a_o^2 - a_i^2)$, where a_i and a_o are the inner and outer disk radii, respectively and i is the inclination[2]. Since the disk is assumed to be a blackbody, the radiation can be described by the Planck function $B_\nu(T_d)$, where T_d is the temperature of the disk. This gives the flux density of the disk

$$F_\nu = \pi\frac{\cos i}{d^2}B_\nu(T_d)(a_o^2 - a_i^2)\,. \tag{3.5}$$

3.1.3 Simple Flat Disk Model

For the flat disk model, it is advisable to start by deriving the disk temperature since it is now assumed to change within the disk. One can imagine the disk as an infinite number of thin rings with radius da (see Fig. 3.1). The incoming radiation hitting the annulus on both the upper and lower surface can therefore be described by

$$P_{in} = 2F_{in}2\pi a\,da\,, \tag{3.6}$$

where $2\pi a\,da$ is the surface area for photons hitting the rings. The disk is assumed to be a blackbody emitting all received radiation by the same surface area from both the upper and lower sides of the disk.

$$P_{out} = 2\sigma T_d^4 2\pi a\,da\,, \tag{3.7}$$

where σ is the Stefan-Boltzmann constant and T is the temperature of the disk. The equilibrium temperature of the disk can then be calculated by a balance between incoming and outgoing radiation $P_{in} = P_{out}$.

$$T_d = \left(\frac{F_{in}}{\sigma}\right)^{1/4} \tag{3.8}$$

[1]Sometimes, the flux density is given in Jansky (Jy), where 1 Jy = 10^{-26} W m^{-2} Hz^{-1}.
[2]At $i = 90°$ the disk appears edge-on, while at $i = 0°$ the disk is face-on.

The incoming radiation F_{in} hitting an accretion disk was first derived by Friedjung (1985) and Adams and Shu (1986). Two assumptions can be made for the flat disk model: the disk height H is zero and the disk is located relatively far away from the star, i.e. $R_* \ll a$. The complete derivation of the incoming flux is shown in Appendix A.

$$F_{in} = \frac{2}{3\pi}\left(\frac{R_*}{a}\right)^3 \sigma T_*^4 \,. \tag{3.9}$$

The temperature of the disk Eq. (3.8) is then given by

$$T_d = \left(\frac{2}{3\pi}\right)^{1/4}\left(\frac{R_*}{a}\right)^{3/4} T_* \,, \tag{3.10}$$

which is also the equation used for the flat disk model derived by Chiang and Goldreich (1997) for T Tauri stars. Similarly to the blackbody disk model, the disk in the flat disk model is assumed to be a blackbody and a point source. The projected emitting area of the annulus is, therefore, $\Omega = 2\pi/d^2 \cos(i) a\, da$ and the spectral flux density can then be written as (Jura, 2003)

$$F_\nu = \frac{2\pi \cos i}{d^2} \int_{a_i}^{a_o} B_\nu(T_d(a))\, a\, da \,. \tag{3.11}$$

The inner and outer disk radii are denoted as a_i and a_o, respectively. The disk is now modelled as a set of rings with radius da, where each ring has a different temperature $T_d(a)$ depending on the distance to the star (see Fig. 3.1). Using the Planck function in wavelength, Eq. (3.4), gives rise to the flux density in terms of wavelength.

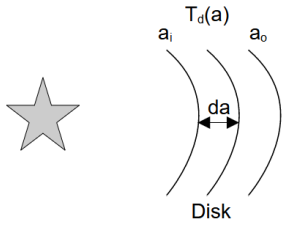

Figure 3.1: Visualization of the flat disk model, where the disk is modelled as a set of rings with different temperatures. Not to scale.

3.1.4 Albedo and Packing Fraction

The flat disk model simplifies the disk to be opaque and perfectly absorbing. To be able to vary the ability of the disk to reflect and emit light, one can multiply two additional parameters to the disk temperature from Eq. (3.10), i.e. albedo and packing fraction. The incoming radiation can be described by $P_{in} = 2(1 - A_b)F_{in} 2\pi a\, da$, where A_b is the albedo

of the disk[3] and the outgoing radiation can be described by $P_{out} = 2\epsilon\sigma T_d^4 2\pi a\, da$, where ϵ is the emissivity of the disk. If the infrared wavelength is assumed to be smaller compared to the debris in the disk, the emissivity can be approximated to be 0.9 (Lissauer and de Pater, 2013, Chapter 4.1.3). Altogether, the disk temperature can then be written as

$$T_d = \left(\frac{2}{3\pi}\right)^{1/4} \left(\frac{R_*}{a}\right)^{3/4} T_* \left(\frac{1-A_b}{\epsilon}\right)^{1/4} . \tag{3.12}$$

To also be able to vary how full the disk is, one can add a packing fraction[4] f. The packing fraction is added to the spectral flux density from Eq. (3.11) as a coefficient.

$$F_\nu = \frac{2\pi\cos i}{d^2} f \int_{a_i}^{a_o} B_\nu(T_d(a))\, a\, da \tag{3.13}$$

Now, one can influence the modelled spectral flux density by varying the inner and outer disk radii, the albedo, or the packing fraction. The integral in Eq. (3.11) and Eq. (3.13) can only be solved numerically.

3.2 Reflected Light

This section focuses on the derivations made for optical reflected light starting with a simple model using a Lambertian surface, followed by a model using the Henyey–Greenstein phase function.

3.2.1 Lambertian Surface

A Lambertian surface is an idealized diffuse reflector. The emergent intensity is therefore described by (Madhusudhan and Burrows, 2012)

$$I = A_b f F_{\text{in}} \frac{\cos i}{\pi} , \tag{3.14}$$

which depends on the inclination or viewing angle of the observer i. F_{in} is the flux hitting the disk, which corresponds to Eq. (3.9) derived for the flat disk model in §3.1.3. It is rewritten as

$$F_{\text{in}} = \frac{2}{3} B_\lambda(T_*) \left(\frac{R_*}{a}\right)^3 \tag{3.15}$$

to have the spectral flux instead of bolometric flux. The total flux density coming from the disk as reflected radiation integrated over $a\, da\, d\psi$ from 0 to 2π is then

$$F_{\text{Lam}} = A_b f \frac{4\cos i}{3d^2} B_\lambda(T_*) R_*^3 \left(\frac{1}{a_i} - \frac{1}{a_o}\right) . \tag{3.16}$$

[3] $A_b = 0$ means the disk absorbs all incoming radiation without reflecting anything. $A_b = 1$ means the disk reflects all incoming radiation without absorbing anything. In this case, the disk temperature is equal to zero.

[4] At $f = 0$ the disk is transparent and $f = 1$ means the disk is opaque.

3.2.2 Henyey–Greenstein Model

A Lambertian surface only describes perfectly diffuse reflected light. For the reflected light of a non-Lambertian surface, one has to take the incident angle α of the light into account. This is done by implementing a phase function $\Phi(\alpha)$

$$I = A_b f \frac{2}{3} B_\lambda(T_*) \left(\frac{R_*}{a}\right)^3 \Phi(\alpha)\,. \tag{3.17}$$

For small particles, one can use the Henyey–Greenstein phase function, which was originally proposed for scattering by interstellar dust (Henyey and Greenstein, 1941). It gives an approximate solution for diffraction effects.

$$\Phi(\alpha) = \frac{1-g^2}{4\pi} \frac{1}{(1+g^2-2g\cos\alpha)^{3/2}}\,, \tag{3.18}$$

The factor of $\frac{1}{4\pi}$ is the normalization constant when normalizing over the solid angle. The asymmetry of the function is described by $-1 \leq g \leq 1$, where $g = 0$ means all radiation is scattered isotropically and $g = 1$ means all radiation is scattered forward. The phase angle α is related to the inclination i by (Madhusudhan and Burrows, 2012)

$$\cos\alpha = \sin(\psi)\sin(i)\,. \tag{3.19}$$

A sketch of the angles is shown in Fig. 3.2. The disk, for example, appears face-on when the inclination is zero. The phase angle in that case is 90°.

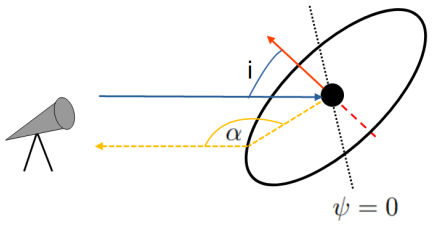

Figure 3.2: Schematic overview over the angles for reflected light. The angle between the normal of the disk and the observer is the inclination i. The orange dashed line shows the phase angle α. The angle ψ goes from 0 to 2π around the whole disk.

The flux density reflected by the disk is then computed similarly to that for the Lambertian surface:

$$F_{\mathrm{HG}} = A_b f \frac{2}{3d^2} B_\lambda(T_*) R_*^3 \left(\frac{1}{a_i} - \frac{1}{a_o}\right) \int_0^{2\pi} \Phi(\alpha) d\psi \tag{3.20}$$

This equation has no analytical solution and can only be solved numerically.

Chapter 4

Results and Discussion

4.1 Infrared Excess

4.1.1 Blackbody and Flat Disk Model

Figure 4.1 shows the blackbody disk model compared to the flat disk model plotted for WD 0145+234 and G 29-38 using the properties displayed in Table 4.1. The disk temperature of the blackbody is chosen to be at 960 K for both disks. The disk in each plot shows up as a smaller peak to the right of the stellar blackbody, which is expected for the infrared excess. One can see how the disk flux density exceeds the stellar flux density at longer wavelengths. This can be explained by Wien's displacement law stating that the temperature and wavelength at a peak in a blackbody spectrum are inversely proportional to each other. A peak at a shorter wavelength has a higher temperature than a peak at a longer wavelength. Additionally, the emitting area of the disk is larger than that of the star. This is why the stellar blackbody is seen as the first peak followed by the disk, which exceeds the star at longer wavelengths.

The left plot shows WD 0145+234, where the blackbody curve and the flat disk model are scaled down by a factor of 0.35 and 0.3, respectively to roughly match the observed flux density by Swan et al. (2024) Figure 2. The right plot shows G 29-38, where only the blackbody curve is scaled down by a factor of 0.8 to roughly match the flux density of Figure 6 in Xu et al. (2018).

Table 4.1: Properties of the white dwarfs WD 0145+234 and G 29-38.

White dwarf	Radius [$R_\odot$]	Temperature [K]	Distance [pc]	Reference
WD 0145+234	0.0116	13060	29.458	Wang et al. (2019)
G 29-38	0.013	11240	17.5	Xu et al. (2018)

One can see that the flat disk curve and the blackbody disk curve overlap well in each plot, which confirms that both models are similar. The blackbody model is a basic but useful attempt to get a general idea of the emitted flux density. But contrary to the flat

disk model, the blackbody model does not have a geometry or a temperature gradient throughout the disk. It can therefore not be used for optical scattering calculations, which will be done later.

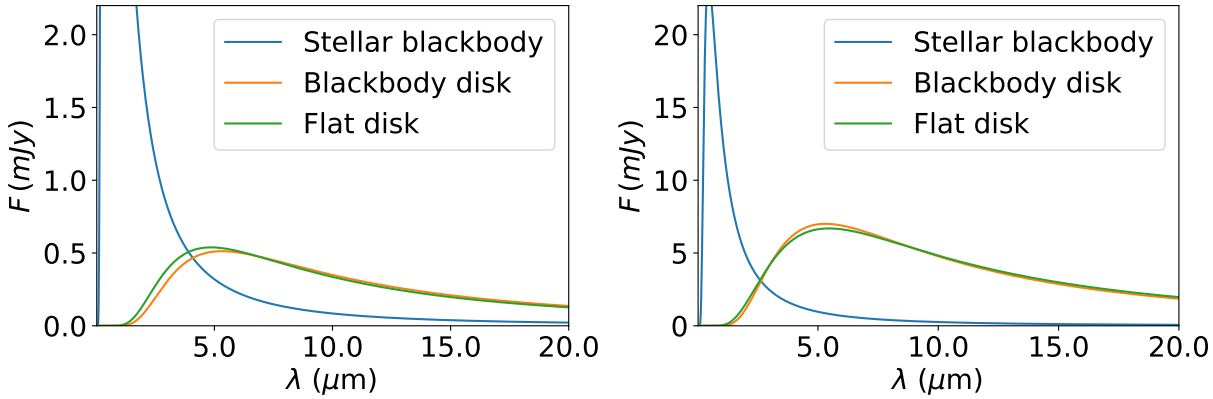

Figure 4.1: The blackbody disk model for WD 0145+234 (left) with inner $a_i = 13R_*$ and outer disk radius $a_o = 24R_*$ (Owens et al., 2023) and G 29-38 (right) with inner and outer disk radius $a_i = 10R_*$ and $a_o = 28R_*$ (Xu et al., 2018) compared to the flat disk model. Both disks have an inclination of 30°.

The difference between both plots is the height and position of the stellar blackbody curve compared to the flat disk model. The left plot, modelling WD 0145+234, is slightly shifted to shorter wavelengths compared to the right plot, which is modelling G 29-38. This behaviour can be explained by the temperature differences of the two stars. Since the white dwarf in the left plot is hotter than the white dwarf in the right plot, the shift to shorter wavelengths is consistent with Wien's displacement law.

Additionally, the left plot is lower in flux density than the plot for G 29-38. This can be explained by the difference in radius and distance of the two white dwarfs. WD 0145+234 has a smaller radius and a larger distance, which with Eq. (3.3) results in a lower flux density. On the other hand, G 29-38 has a larger radius and smaller distance leading to a higher flux density, which can be seen in the plots.

4.1.2 Varying Disk Radii

In this section, I increase and decrease the inner and outer disk radii systematically to look at a variety of disks. Figure 4.2 shows a schematic overview of the sizes and distances of the disks considered in the plots in Fig. 4.3 and 4.4. The albedo and packing fraction are kept constant at 0 and 1 and the disk is assumed to be face-on, i.e. $i = 0°$.

The plots in Fig. 4.3 show G 29-38 and its debris disk for different inner disk radii a_i, while keeping the outer radius constant at $a_o = 28R_*$. This corresponds to a disk similar to the one shown in A in Fig. 4.2. The left plot shows disks with small inner radii. One can see that decreasing the inner disk radius increases the peak height. Additionally, the peak shifts to the left. Decreasing the inner disk radius while keeping the outer radius

constant, increases the surface area of the disk. Since the disk has more surface area it can absorb more radiation leading to an increase in flux density and therefore a higher peak. Furthermore, the disk is very close to the white dwarf for small inner radii, leading to the disk becoming very hot. Hence, the peaks are shifted to shorter wavelengths.

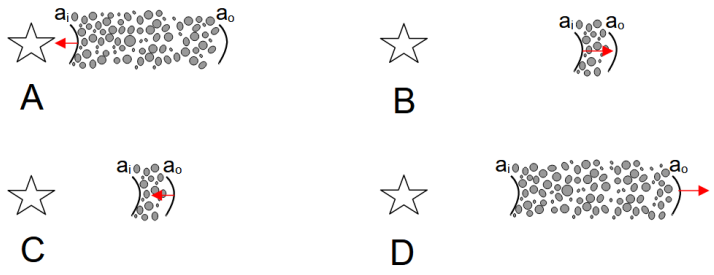

Figure 4.2: Schematic overview of the different sizes and distances of the disks considered in the above plots. The red arrow symbolizes which radius is being changed for the different scenarios.

The plot on the right-hand side shows disks with large inner radii (Fig. 4.2, B). The peak decreases with increasing inner radius and shifts slightly to the right. The debris disk is further away from the white dwarf than before and has a small surface area. Because of that, the disk is cooler and absorbs less radiation, leading to the peak being lower in height and shifted to longer wavelengths.

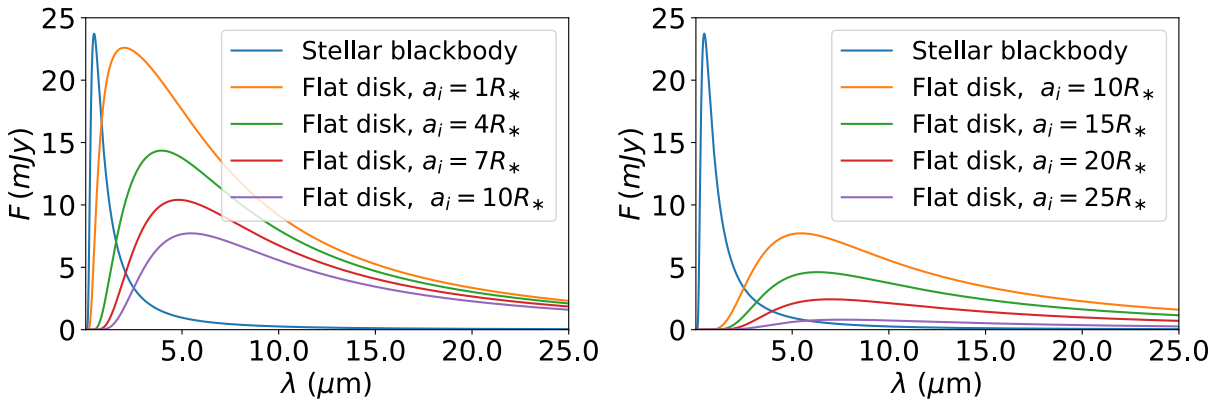

Figure 4.3: The flat disk model plotted for G 29-38 with outer disk radius $a_o = 28R_*$ (Xu et al., 2018) and varying inner disk radius a_i.

Figure 4.4 shows plots of G 29-38 its debris disk with inner disk radius $a_i = 10R_*$ and different outer disk radii. The plot on the left-hand side shows disks with small outer radii (Fig. 4.2, C). One can see that the peak height decreases with decreasing outer radius. The surface area of the disk is smaller for smaller outer radii and therefore the disk emits

less flux density. The peaks are shifted to the shorter wavelengths, which means the disk becomes hotter for small outer radii. While the inner disk edge has the same distance to the star, now the outer disk edge is closer than before, leading to the outer disk edge being hotter and thus causing the disk temperature to become hotter on average.

The plot on the right-hand side shows the debris disk for larger outer radii while keeping the inner radius constant (Fig. 4.2, D). The peak heights increase with increasing radius, which is due to the disk getting a larger surface area for larger outer radii. In addition to that the peaks shift to longer wavelengths, meaning the disk becomes colder. The outer edge of the disk moves further away with increasing outer radius, which leads to the outer edge being cooler than before. This in turn leads to the disk temperature becoming cooler on average as well.

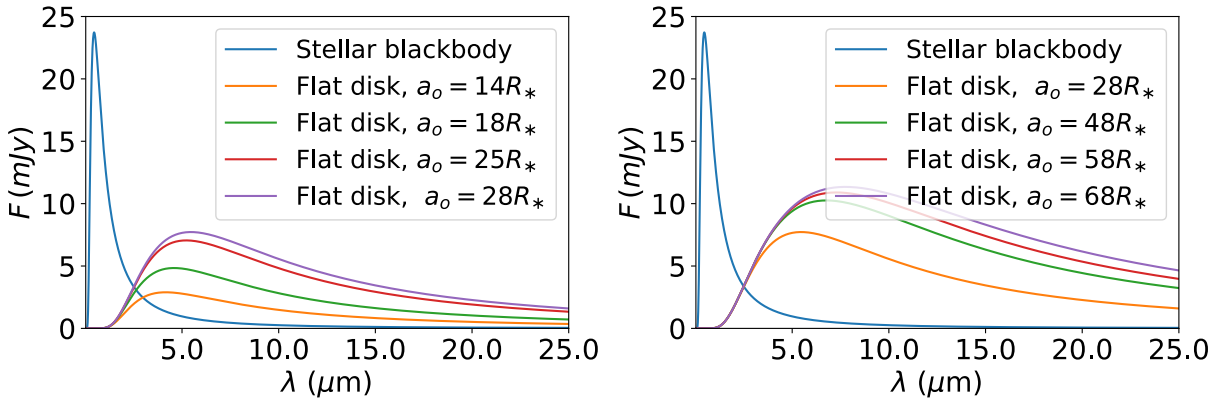

Figure 4.4: The flat disk model plotted for G 29-38 with inner disk radius $a_i = 10R_*$ (Xu et al., 2018) and varying outer disk radius a_o.

One can conclude that simply changing the radius gives a variety of flux density values. To achieve very high values for the flux density, the disk radius needs to be large. To get a high flux density at a low wavelength, the inner disk edge needs to be close to the star, while the outer disk edge is far enough to have a large surface area (Fig. 4.2, A). Similarly, to get a high flux at a long wavelength, the disk needs to be away from the star while having a large outer radius (Fig. 4.2, D). For low flux density values, the disk radius has to be small. For a peak at short wavelengths the disk has to be close to the star (Fig. 4.2, C), while for a peak at long wavelengths, the disk has to be further away (Fig. 4.2, B). During the derivations of the flat disk model R_*/a is assumed to be small. Therefore, the extreme case A, where the disk inner radius is very small, will not work for this model.

4.1.3 Albedo and Packing Fraction

Figure 4.5 (left) shows the flat disk model for WD 0145+234 with varying albedo values. One can see that decreasing the albedo increases the peak height of the flat disk model. A higher albedo means more radiation is reflected, while a zero albedo means all radiation

hitting the disk is absorbed. Therefore, the highest peak in the plot is for $A_b = 0$ and the lowest curve is not visible due to the disk reflecting all radiation at $A_b = 1$.

By taking a close look at the positions of each peak, it is noticeable how increasing the albedo also slightly shifts the peaks to shorter wavelengths. As the albedo increases the disk starts to reflect more radiation than it absorbs. This causes the disk to become cooler. Hence, the peaks for higher albedo values are shifted to larger wavelengths.

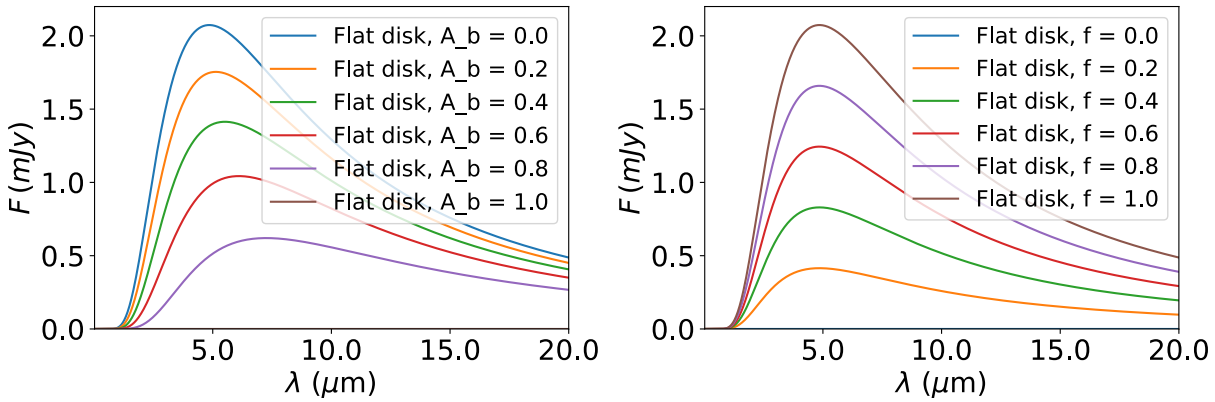

Figure 4.5: The flat disk model plotted for WD 0145+234 with inner disk radius $a_i = 13R_*$ and outer disk radius $a_o = 24R_*$ (Owens et al., 2023). The left plot shows the debris disk for different albedo values, while the right plot shows the disk for different packing fractions. The disk is assumed to be face-on.

On the right-hand side of Fig. 4.5, one can see the flat disk model for WD 0145+234 with varying packing fractions. A high packing fraction corresponds to more material in the disk, while a zero packing fraction describes a transparent disk. The peak heights decrease with decreasing packing fraction, which is consistent with the definition of the packing fraction as a parameter describing the amount of material in the disk. Less material means the disk can absorb less radiation causing the peak to be lower.

All in all, to change the flux density one can increase or decrease the packing fraction to get higher or lower peak heights. By changing the albedo, the peaks also slightly shift. A higher albedo will lower the peak height and move it to a higher wavelength.

4.2 Reflected Visible Light

4.2.1 Lambertian Surface

Starting with the Lambertian reflector five parameters can be varied for this model: inner and outer radius, albedo, packing fraction, and inclination. Changing the inclination changes the reflected flux density due to the dependence on cosine. At zero-degree inclination, the disk appears face-on, which leads to a maximum flux density being reflected

by the disk. If the disk is edge-on, i.e. $i = 90°$, no flux density is reflected to the observer, which is why there is no curve for 90° in Fig. B.1 [Appendix B].
Figure 4.6 shows the ratio between the reflected light and the stellar blackbody depending on packing fraction and albedo. The inclination is fixed at 0° and the inner and outer radii are $a_i = 10R_*$ and $a_o = 28R_*$ respectively. The ratio is about 1% for small albedo and packing fraction values. For high albedo and packing fractions, the ratio reaches about 2.8%. This is expected from Eq. (3.16) since both the albedo and packing fraction are a multiplicative factor for the flux density. The disk is less reflective for low albedo values and therefore the flux density is low. Additionally, an almost transparent disk will also reflect less radiation leading to a low flux density. Typical albedo values are around 0.1-0.2 for asteroids (Warner et al., 2009). Therefore, the ratio between the reflected light and the stellar blackbody can be expected to be around 0.4% for G 29-38.

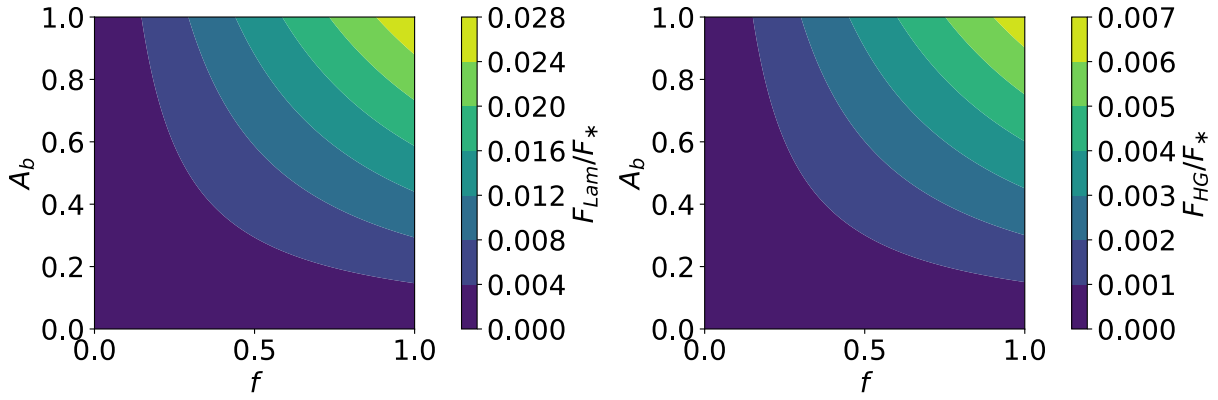

Figure 4.6: A contour plot for the ratio between the Lambertian reflected light and the stellar radiation of white dwarf G 29-38 for $i = 0°$ on the left-hand side. The right-hand side shows the same plot but for the HG model using $g = 0.1$ and $i = 0°$. The x-axis shows the packing fraction, while the y-axis shows the albedo.

Changing the inner and outer disk radii as in §4.1.2, similarly changes the reflected flux density. The left plot in Fig. B.2 in Appendix B shows disks with varying inner radius, while the outer radius is kept constant at $a_o = 28R_*$. Decreasing the inner radius leads to a higher flux density reflected by the disk. Since the outer radius is kept constant, the disk increases in size when decreasing the inner radius. Additionally, the disk is closer to the star for smaller inner radii, which by the inverse square law gives a higher flux density.

The right plot in Fig. B.2 in Appendix B shows plots for different outer radii while the inner radius is kept at $a_i = 10R_*$. The outer disk radius does not affect the flux density as much as the inner disk radius, as seen when comparing the left and right plots. By decreasing the inner disk edge, the disk moves closer to the star leading to a higher flux density. By only moving the outer disk edge, the closest distance from the star to the disk does not change, and hence the flux density does not change much.

4.2.2 Henyey–Greenstein Model

A Lambertian surface is a simplified model and does not take diffraction effects into account. For a more realistic model of reflected light one can use the HG phase function. A plot of the HG phase function as a function of α for varying g is shown in Fig. B.3 in Appendix B. It shows the directional dependence of scattering for different g and α values. Looking at the left plot, which is showing negative g-values and therefore backwards scattering, one can see that the phase function has a peak for large α. As α gets smaller $\Phi(\alpha, g)$ decreases indicating that less light is scattered forward. This behavior is expected as this plot for negative g-values indicates a strong preference for backwards scattering. The right plot shows positive g-values and therefore forward scattering. This time the phase function peaks for low α and decreases as α increases, which shows that less light is scattered backwards. The phase function behaves as a forward scattering phase function, which is expected for positive g-values. Lastly, The phase angle α does not matter for $g \approx 0$. The phase function stays flat for all phase angles, indicating that the scattering is uniform in all directions, which is expected for the HG phase function as $g = 0$ describes isotropic scattering.

Figure 4.7 shows the reflected light with this phase function compared to the Lambertian for both white dwarfs from Table 4.1. The height difference can be explained by the difference in the stellar properties, as already done for the infrared excess in §4.1.1. The Lambertian reflector is higher than the HG-phase function since a Lambertian surface is a perfectly diffuse scatterer.

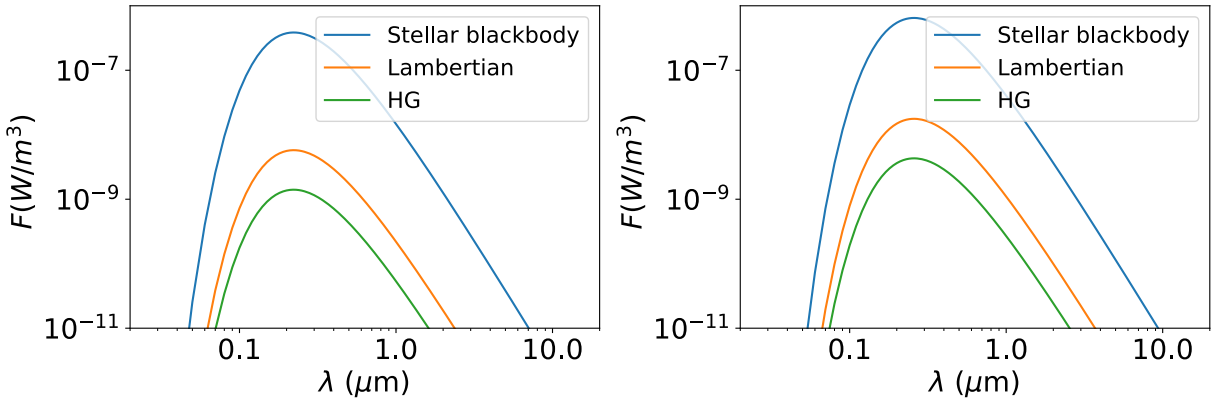

Figure 4.7: Plots of the reflected light using the Henyey-Greenstein phase function compared to the Lambertian surface for g = 0.1 and i = 0°. The left plot shows WD 0145+234 and the right plot shows G 29-38.

The HG model has six parameters that can be varied, where five of these are the same ones as for the Lambertian. The sixth parameter is the g-value, which indicates if the radiation is scattered backwards, isotropic, or forwards. The reflected flux density decreases, by increasing the g-value of the phase function, which is shown in Fig. 4.8 (left). The disk is assumed to be face-on. A higher g-value means more radiation is scattered forward

and therefore less radiation is detected. For $g = 0$ (isotropic scattering), the HG reflected flux is a factor of 4 smaller than the Lambertian. This factor arises since the perfectly diffuse nature of Lambertian scattering is not the same as the isotropic nature of $g = 0$ Henyey–Greenstein scattering.

The inclination does not have a strong impact on the phase function reflected flux, as can be seen in Fig. 4.8 (right). For $i = 0°$ the ratio between the reflected and stellar flux is the lowest while for $i = 90°$ it is the highest. This is because of the dependence on sine. The behaviour of i here is therefore opposite to the behaviour of i in the Lambertian reflector, where i depends on cosine.

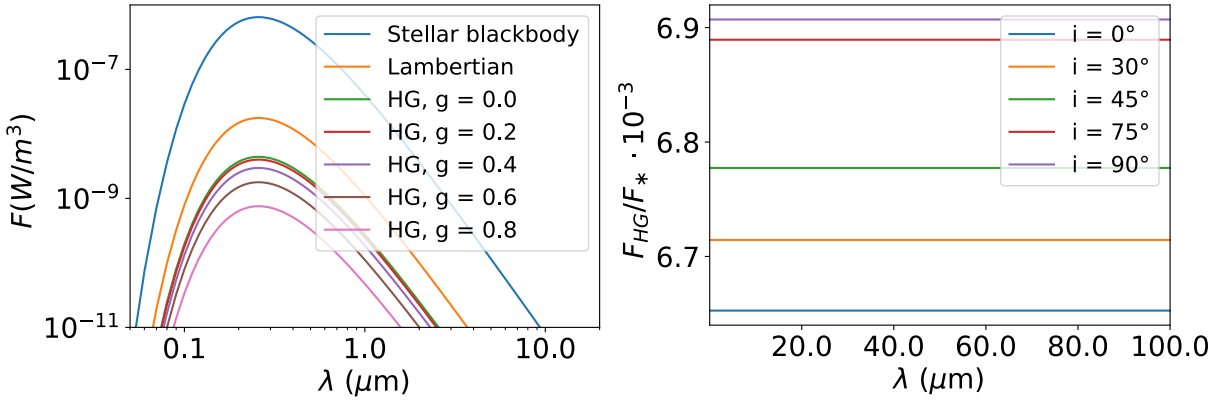

Figure 4.8: The reflected light with phase function for different g-values (left) for G 29-38. The inclination is kept at $i = 0°$. The right plot shows the ratio of reflected and stellar light for G 29-38 for different inclinations when $g = 0.1$.

The HG reflected flux follows the same behaviour as the Lambertian reflected flux for different albedo and packing fractions, namely the reflected flux density is maximized for maximum A_b and f and vice versa. However, the ratio between reflected and stellar flux density is smaller because, as seen in Fig. 4.7, the Lambertian reflected flux is higher than the reflected flux described by the HG-phase function. A realistic value for the ratio between reflected flux and stellar radiation of G 29-38 described by the HG-phase function when almost all radiation is scattered isotropically is about 0.1%, as shown in a contour plot in Fig. 4.6 (right).

Lastly, changing the inner and outer radius for the HG model changes the flux density similarly to the Lambertian model. Decreasing the inner radius increases the reflected flux density due to the inverse square law. The ratios are again smaller since the reflected flux with the HG phase function is lower than the Lambertian reflected flux. The plots are shown in Fig. B.4 in Appendix B.

4.3 Variability

Now that the effect of each parameter on each model has been studied in detail, one can apply this knowledge to the variability of white dwarf debris disks. The focus of this section

is to look at the flux changes observed by Swan et al. (2024) for WD 0145+234 (see Fig. 2.2, right) and find parameters for the flat disk model that roughly match the observations. In doing so, I try to match two flux values from Figure 1 (Swan et al., 2024) at 4.5 μm using the flat disk model. I chose the first value at 1.48 mJy and the second one at 0.51 mJy, which were observed with a three-year distance by Swan et al. (2024). I then use these parameters to plot the reflected light and examine how the infrared variability affects it.

4.3.1 Infrared Excess

Firstly, the albedo is chosen to be constant at 0.2 since this is a typical value for asteroids (Warner et al., 2009). The flat disk model can match the first value chosen by having a disk that is 100% filled and has an inner and outer radius of $a_i = 13R_*$ and $a_o = 24R_*$, respectively. The second value can be matched by decreasing the packing fraction to 35%. Note that, these values are not unique, since a completely different set of parameters could also give the same flux values. A plot of both sets of parameters is shown in Fig. 4.9.

Table 4.2: Parameters for the infrared excess values observed by Swan et al. (2024) at 4.5 μm. The albedo is kept constant at 0.2 and the inclination is 30°.

Flux [mJy]	Packing fraction	Inner radius [R_*]	Outer radius [R_*]
1.48	1	13	24
0.51	0.35	13	24

The flat disk model fits the decrease in flux well by simply changing the packing fraction. The cause of the reduction in flux and packing fraction could be collisional grinding, which is typical of debris disks (Wyatt et al., 2007; Wyatt, 2008).

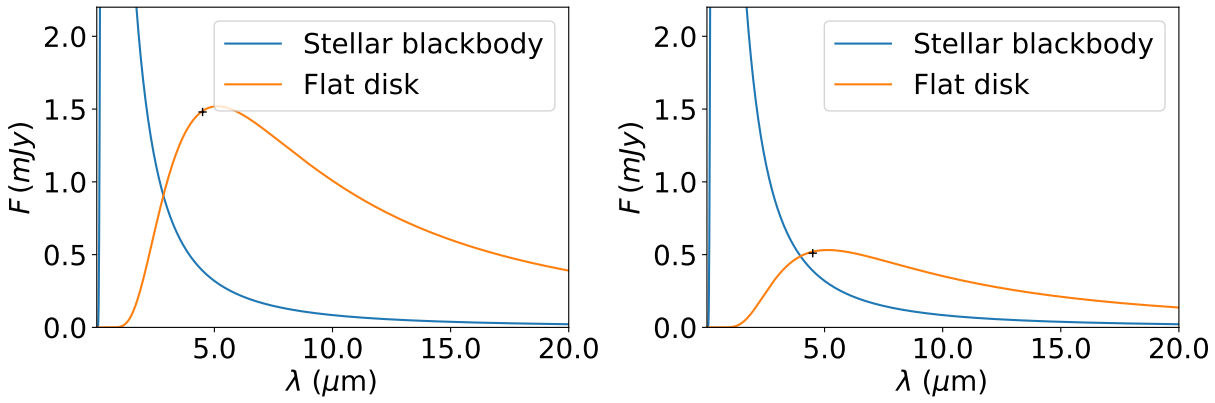

Figure 4.9: The infrared excess of WD 0145+234 for the first parameters simulating 1.48 mJy (left) and the second parameters simulating 0.51 mJy (right). The black crosses indicate the values observed by Swan et al. (2024).

4.3.2 Reflected Light

For the same values from Table 4.2 one can now take a look at the reflected light coming from the disk. The plots are shown in Fig. 4.10. From the first to the second set of parameters, namely on a timescale of about three years, the reflected flux coming from the disk decreases by a factor of 3. The ratio between the Lambertian reflected light and stellar radiation is about 0.3% for the first set of parameters and becomes 0.09% for the second set of parameters. However, a Lambertian surface is a simplified model for reflected light. The HG model is a better estimation of the actual reflected light. For these plots, the disk is assumed to be face-on and about half the radiation is scattered forward. The ratios for the HG reflected flux and stellar radiation are about 0.07% for the first and 0.03% for the second set of parameters. These values are very small compared to the expected ratios for G 29-38 from Fig. 4.6. However, G 29-38 is larger in radius compared to WD 0145+234 which would lead to a larger flux density, and hence the reflected light from the disk would make up a larger fraction of stellar radiation.

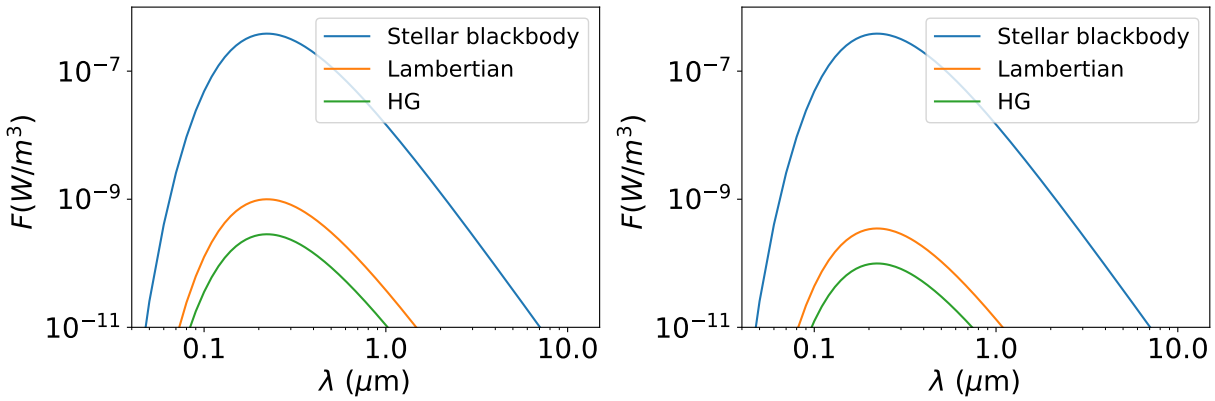

Figure 4.10: The reflected light of WD 0145+234 for the first (left) and second (right) set of parameters in Table 4.2. The disk is assumed to scatter almost all radiation isotropically $g = 0.1$.

Chapter 5

Conclusion and Outlook

In summary, I studied infrared and reflected light from disks around white dwarfs. In doing so I derived mathematical models for the disks and studied their parameters in detail. Lastly, I looked at the variability of the disks in both infrared and visible wavelengths to examine whether one can detect any change in the disks in optical photometry, which is a gap in current research.

I derived two models for the infrared excess. The blackbody disk model appeared as a useful attempt to get a general idea of the flux density coming from the disk. Since this model has no geometry, it cannot be used for optical scattering and hence the flat disk model was derived. Modelled as a set of rings, where each ring has a different temperature depending on the distance to the star, this model is a better approximation for the infrared excess and a useful tool for optical scattering. By adding an albedo and packing fraction to the flat disk model, the disk reflectivity and opacity can be varied.

For the reflected light, I started by looking at a Lambertian surface, which assumes the disk to be a perfectly diffuse scatterer. Additionally to the radii, albedo, and packing fraction, the model for the Lambertian reflector also depends on the inclination. A face-on disk leads to a maximum flux density, while an edge-on disk has no flux density being reflected. Each variable parameter only scales the blackbody curve down or up and does not shift it to higher or shorter wavelengths, since it is always the same blackbody.

The last model I looked at, was a model for the reflected light using the Henyey-Greenstein phase function. The Lambertian model is at higher flux densities than the HG model due to the HG phase function taking diffraction effects into account. The g-value of the phase function describes the direction of scattering of the reflected light going from -1 being backward scattering to 1 forward scattering. At zero the phase function is scattering isotropically, which leads to a high flux density. The parameters from the Lambertain model affect this model in a similar way.

Lastly, I investigated the infrared variability by taking two values observed three years apart by Swan et al. (2024) for WD 0145+234, and finding suitable parameters for the flat disk model to get similar values. I fixed the albedo at 0.2 and the inner and outer radius at $a_i = 13R_*$ to $a_o = 24R_*$ and found that from one flux value to another the packing fraction decreased from 100% to 35%. However, these values are not unique since a different set of

parameters can simulate the observed flux density values as well.

Using this set of parameters, I lastly plotted the reflected light for the Lambertian and HG models. The decrease in flux seen for the infrared excess is also seen in the reflected light for both models. The reflected light changes by a factor of three in three years. However, it only makes up a small fraction of the stellar light. For the ratio of reflected light using the HG model and stellar radiation, the value is about 0.07% and decreases to 0.03%.

For future research, one can discuss more complicated disk models than the flat disk model to study the infrared excess. The emissivity introduced to the flat disk model derived here has the assumption that the dust grains are larger than the wavelength. However, in a real disk, one would expect several different-sized grains. Since the emissivity depends on the grain size one could use a distribution of grain sizes to get a more accurate value of it than just having a constant value. The HG model for reflected light also assumes a constant grain size, where all debris is larger than the wavelength. This is also not true for all debris and dust in the disk and a more advanced scattering phase function could be taken into account instead. All plots for the reflected light have the same blackbody but in practice, it also depends on wavelength. To advance the model for reflected light further, this could be taken into account.

While the flat disk model can explain the infrared variability when allowing changes in the packing fraction, one could be able to describe the processes leading to variations in flux in better detail using different models with more complex geometries. To explain and investigate the infrared variability further, one could think about a model for the debris and the gas together. Both disks are in the same region and are related to one another due to effects like PR-drag, Yarkovsky effect, collisions, and sublimation.

The reflected light from a white dwarf debris disk has not been observed yet. For future research, one can try to see if the reflected light can be observed. To do so, one could think about blocking out the light coming from the star as it is done for protoplanetary disks or disks around MS stars. A great example of this method is the Fomalhaut disk or the β Pictoris system, where the stellar light is blocked out by using a coronagraph to see the disk (Lawson et al., 2024; Apai et al., 2015). However, the disks observed using this method are far away from their host star. Debris disks of white dwarfs are usually very close to the star, which makes observing the reflected light with this method unfavourable.

Instead, one could think about observing the unresolved flux from the white dwarf and the disk around it. If the disk changes, the reflected flux from the disk will change, which in turn also slightly changes the total observed flux. One could then see the change relative to the previous flux value over time scales of months or years. But one has to consider that the reflected flux is only a small fraction of the stellar light and that for example, the factor of three change for WD 0145+234 happened in three years. In general, the observability depends on the magnitude of the star. Therefore a closer white dwarf with a disk that reflects a larger portion of incoming light might be more favorable to observe.

To do so, one would need a stable telescope, low noise, and a good calibration against the background. This would also include a suitable selection of companion stars to cali-

brate the photometer. Additionally, one must ensure that the variations come from the target star and not the background or a companion star. In general, relative photometry would be suitable such that the absolute stability of the telescope does not matter. Furthermore, multiple exposures from one night could be taken to increase the signal-to-noise ratio. Suitable telescopes could be CHEOPS, TESS, or PLATO, and also the Vera Rubin Observatory.

In conclusion, I studied the infrared and optical light of white dwarf debris disks using mathematical models. Using the parameters found for the infrared variability of WD 0145+234, I studied how the reflected light would be expected to change and what fraction of the stellar radiation it constitutes. Using the models I derived for the reflected light, I found that the reflected light changes by a factor of three in three years for WD 0145+234 and that it makes up about 0.07% to 0.03% of stellar radiation. By using relative photometry and very good calibration one could try to observe the reflected light coming from a white dwarf debris disks, which is a gap in current research. Observations of reflected light can in example give insight into the size, composition and surface properties (albedo) of the disks. In general, reflected light could give complementary information to already existing detection methods.

Acknowledgments

Firstly, I want to thank my supervisors Alexander Mustill and Judith Korth for all their support throughout my project. I am deeply grateful for your expertise and feedback. Next, I want to thank the friends I made at Lund University for all the fun discussions we shared and all the moral support. A special thank you goes to Mahmoud for helping me debug my code and for all the continuous support and belief in me. Thank you to Verena, Evi, and Warsame, whom I could turn to when I felt stuck on a problem, and to Niklas and Fiona for their support and genuine interest in my thesis. Then, I want to thank my family for their support throughout my studies. Lastly, I want to thank Anna Arnadottir for allowing me to work at the planetarium. It was an unique experience and I enjoyed educating the public about the wonders of space.

List of Abbreviations

HG Henyey–Greenstein
MS Main–Sequence
SED Spectral Energy Distribution

Bibliography

Adams, F. C. and Shu, F. H. (1986). Infrared Spectra of Rotating Protostars.

Apai, D., Schneider, G., Grady, C. A., Wyatt, M. C., Lagrange, A.-M., Kuchner, M. J., Stark, C. J., and Lubow, S. H. (2015). The Inner Disk Structure, Disk-Planet Interactions, and Temporal Evolution in the β Pictoris System: A Two-epoch HST/STIS Coronagraphic Study. *ApJ*, 800(2):136.

Ballering, N. P., Levens, C. I., Su, K. Y. L., and Cleeves, L. I. (2022). The Geometry of the G29-38 White Dwarf Dust Disk from Radiative Transfer Modeling. *ApJ*, 939(2):108.

Bonsor, A., Mustill, A. J., and Wyatt, M. C. (2011). Dynamical effects of stellar mass-loss on a Kuiper-like belt. *MNRAS*, 414(2):930–939.

Bonsor, A. and Wyatt, M. (2010). Post-main-sequence evolution of A star debris discs. *MNRAS*, 409(4):1631–1646.

Chiang, E. I. and Goldreich, P. (1997). Spectral Energy Distributions of T Tauri Stars with Passive Circumstellar Disks. *ApJ*, 490(1):368–376.

Demtröder, W. (2017). *Scattering by Micro-particles; Mie-Scattering*, chapter 10.9.3. Springer Nature Switzerland AG 2019.

Dennihy, E., Clemens, J. C., Dunlap, B. H., Fanale, S. M., Fuchs, J. T., and Hermes, J. J. (2018). Rapid Evolution of the Gaseous Exoplanetary Debris around the White Dwarf Star HE 1349-2305. *ApJ*, 854(1):40.

Dennihy, E., Debes, J. H., Dunlap, B. H., Dufour, P., Teske, J. K., and Clemens, J. C. (2016). A Subtle Infrared Excess Associated with a Young White Dwarf in the Edinburgh-Cape Blue Object Survey. *ApJ*, 831(1):31.

Farihi, J. (2016). Circumstellar debris and pollution at white dwarf stars. *NAR*, 71:9–34.

Friedjung, M. (1985). Accretion disks heated by luminous central stars. *A&A*, 146:366–368.

Henyey, L. G. and Greenstein, J. L. (1941). Diffuse radiation in the Galaxy. *ApJ*, 93:70–83.

Jura, M. (2003). A Tidally Disrupted Asteroid around the White Dwarf G29-38. *ApJ*, 584(2):L91–L94.

Jura, M., Farihi, J., Zuckerman, B., and Becklin, E. E. (2007). Infrared Emission from the Dusty Disk Orbiting GD 362, an Externally Polluted White Dwarf. *AJ*, 133(5):1927–1933.

Karttunen, H., Kröger, P., Oja, H., Poutanen, M., and Donner, K. J. (2017). *Albedos*, chapter 7.8, pages 161–162. Springer Berlin Heidelberg.

Koester, D. (2009). Accretion and diffusion in white dwarfs. New diffusion timescales and applications to GD 362 and G 29-38. *A&A*, 498(2):517–525.

Lawson, K., Schlieder, J. E., Leisenring, J. M., Bogat, E., Beichman, C. A., Bryden, G., Gáspár, A., Groff, T. D., McElwain, M. W., Meyer, M. R., Barclay, T., Calissendorff, P., De Furio, M., Li, Y., Rieke, M. J., Ygouf, M., Greene, T. P., Girard, J. H., Gennaro, M., Kammerer, J., Rest, A., Roellig, T. L., and Sunnquist, B. (2024). JWST/NIRCam Detection of the Fomalhaut C Debris Disk in Scattered Light. *arXiv e-prints*, page arXiv:2405.00573.

Lissauer, J. J. and de Pater, I. (2013). *Fundamental Planetary Science: Physics, Chemistry and Habitability*. Cambridge University Press.

Lockwood, D. J. (2019). *Rayleigh and Mie Scattering*, pages 1–12. Springer Berlin Heidelberg.

Madhusudhan, N. and Burrows, A. (2012). Analytic Models for Albedos, Phase Curves, and Polarization of Reflected Light from Exoplanets. *ApJ*, 747(1):25.

Maldonado, R. F., Villaver, E., Mustill, A. J., Chavez, M., and Bertone, E. (2020a). Dynamical evolution of two-planet systems and its connection with white dwarf atmospheric pollution. *MNRAS*, 497(4):4091–4106.

Maldonado, R. F., Villaver, E., Mustill, A. J., Chavez, M., and Bertone, E. (2020b). Understanding the origin of white dwarf atmospheric pollution by dynamical simulations based on detected three-planet systems. *MNRAS*, 499(2):1854–1869.

McDonald, C. H. and Veras, D. (2023). Binary asteroid scattering around white dwarfs. *MNRAS*, 520(3):4009–4022.

Owens, D., Xu, S., Manjavacas, E., Leggett, S. K., Casewell, S. L., Dennihy, E., Dufour, P., Klein, B. L., Yeh, S., and Zuckerman, B. (2023). Disk or Companion: Characterizing Excess Infrared Flux in Seven White Dwarf Systems with Near-infrared Spectroscopy. *AJ*, 166(1):5.

Paquette, C., Pelletier, C., Fontaine, G., and Michaud, G. (1986). Diffusion in White Dwarfs: New Results and Comparative Study. , 61:197.

Prialnik, D. (2010). *Thermal pulses and the asymptotic giant branch*, chapter 9.6, pages 226–230. Cambridge University Press.

Reach, W. T., Kuchner, M. J., von Hippel, T., Burrows, A., Mullally, F., Kilic, M., and Winget, D. E. (2005). The Dust Cloud around the White Dwarf G29-38. *ApJ*, 635(2):L161–L164.

Ruden, S. P. and Pollack, J. B. (1991). The Dynamical Evolution of the Protosolar Nebula. *ApJ*, 375:740.

Rutten, R. J. (2003). *Radiative Transfer in Stellar Atmospheres*, chapter 2.1, page 9. Sterrekundig Instituut Utrecht Institute of Theoretical Astrophysics Oslo.

Steele, A., Debes, J., Xu, S., Yeh, S., and Dufour, P. (2021). A Characterization of the Circumstellar Gas of WD 1124-293 Using Cloudy. *ApJ*, 911(1):25.

Swan, A., Farihi, J., Su, K. Y. L., and Desch, S. J. (2024). The first white dwarf debris disc observed by JWST. *MNRAS*, 529(1):L41–L46.

Swan, A., Farihi, J., and Wilson, T. G. (2019). Most white dwarfs with detectable dust discs show infrared variability. *MNRAS*, 484(1):L109–L113.

Swan, A., Farihi, J., Wilson, T. G., and Parsons, S. G. (2020). The dust never settles: collisional production of gas and dust in evolved planetary systems. *MNRAS*, 496(4):5233–5242.

Swan, A., Kenyon, S. J., Farihi, J., Dennihy, E., Gänsicke, B. T., Hermes, J. J., Melis, C., and von Hippel, T. (2021). Collisions in a gas-rich white dwarf planetary debris disc. *MNRAS*, 506(1):432–440.

Vanderbosch, Z. P., Rappaport, S., Guidry, J. A., Gary, B. L., Blouin, S., Kaye, T. G., Weinberger, A. J., Melis, C., Klein, B. L., Zuckerman, B., Vanderburg, A., Hermes, J. J., Hegedus, R. J., Burleigh, M. R., Sefako, R., Worters, H. L., and Heintz, T. M. (2021). Recurring Planetary Debris Transits and Circumstellar Gas around White Dwarf ZTF J0328-1219. *ApJ*, 917(1):41.

Vanderburg, A., Rappaport, S. A., Xu, S., Crossfield, I. J. M., Becker, J. C., Gary, B., Murgas, F., Blouin, S., Kaye, T. G., Palle, E., Melis, C., Morris, B. M., Kreidberg, L., Gorjian, V., Morley, C. V., Mann, A. W., Parviainen, H., Pearce, L. A., Newton, E. R., Carrillo, A., Zuckerman, B., Nelson, L., Zeimann, G., Brown, W. R., Tronsgaard, R., Klein, B., Ricker, G. R., Vanderspek, R. K., Latham, D. W., Seager, S., Winn, J. N., Jenkins, J. M., Adams, F. C., Benneke, B., Berardo, D., Buchhave, L. A., Caldwell, D. A., Christiansen, J. L., Collins, K. A., Colón, K. D., Daylan, T., Doty, J., Doyle, A. E., Dragomir, D., Dressing, C., Dufour, P., Fukui, A., Glidden, A., Guerrero, N. M., Guo, X., Heng, K., Henriksen, A. I., Huang, C. X., Kaltenegger, L., Kane, S. R., Lewis, J. A., Lissauer, J. J., Morales, F., Narita, N., Pepper, J., Rose, M. E., Smith, J. C., Stassun, K. G., and Yu, L. (2020). A giant planet candidate transiting a white dwarf. *Nature*, 585(7825):363–367.

Veras, D. (2020). The white dwarf planet WD J0914+1914 b: barricading potential rocky pollutants? *MNRAS*, 493(4):4692–4699.

Veras, D., Eggl, S., and Gänsicke, B. T. (2015a). The orbital evolution of asteroids, pebbles and planets from giant branch stellar radiation and winds. *MNRAS*, 451(3):2814–2834.

Veras, D., Higuchi, A., and Ida, S. (2019). Speeding past planets? Asteroids radiatively propelled by giant branch Yarkovsky effects. *MNRAS*, 485(1):708–724.

Veras, D., Leinhardt, Z. M., Eggl, S., and Gänsicke, B. T. (2015b). Formation of planetary debris discs around white dwarfs - II. Shrinking extremely eccentric collisionless rings. *MNRAS*, 451(4):3453–3459.

Veras, D., McDonald, C. H., and Makarov, V. V. (2020). Constraining the origin of the planetary debris surrounding ZTF J0139+5245 through rotational fission of a triaxial asteroid. *MNRAS*, 492(4):5291–5296.

Veras, D., Mustill, A. J., and Bonsor, A. (2024). The evolution and delivery of rocky extra-solar materials to white dwarfs. *arXiv e-prints*, page arXiv:2401.08767.

Wang, T.-g., Jiang, N., Ge, J., Cutri, R. M., Jiang, P., Sheng, Z., Zhou, H., Bauer, J., Mainzer, A., and Wright, E. L. (2019). An Ongoing Mid-infrared Outburst in the White Dwarf 0145+234: Catching in Action the Tidal Disruption of an Exoasteroid? *ApJ*, 886(1):L5.

Warner, B. D., Harris, A. W., and Pravec, P. (2009). The asteroid lightcurve database. *Icarus*, 202(1):134–146.

Wyatt, M. C. (2008). Evolution of debris disks. *ARA&A*, 46:339–383.

Wyatt, M. C., Smith, R., Su, K. Y. L., Rieke, G. H., Greaves, J. S., Beichman, C. A., and Bryden, G. (2007). Steady State Evolution of Debris Disks around A Stars. *ApJ*, 663(1):365–382.

Xu, S., Su, K. Y. L., Rogers, L. K., Bonsor, A., Olofsson, J., Veras, D., van Lieshout, R., Dufour, P., Green, E. M., Schlawin, E., Farihi, J., Wilson, T. G., Wilson, D. J., and Gänsicke, B. T. (2018). Infrared Variability of Two Dusty White Dwarfs. *ApJ*, 866(2):108.

Zuckerman, B. and Becklin, E. E. (1987). Excess infrared radiation from a white dwarf—an orbiting brown dwarf? *Nature*, 330(6144):138–140.

Appendix A

Derivation of the Incoming Flux

This section is about the derivation for the flux hitting the disk originally derived by Friedjung (1985) and Adams and Shu (1986). This derivation is done according to a paper by Ruden and Pollack (1991). For a flat debris disk, one can imagine a very thin and flat disk. This means the disk height H is zero. To describe the geometries of the system spherical coordinates are used, where the origin is set at the disk such that the polar axis is along the distance a between the star and the disk.

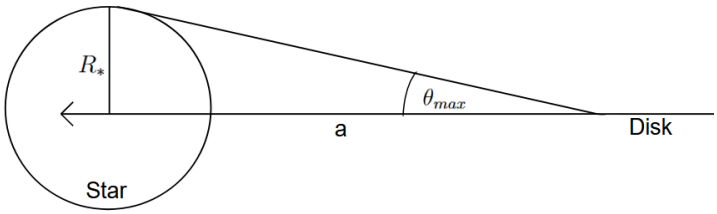

Figure A.1: Geometries of the flat debris disk model. Not to scale.

The incoming flux F_{in} can then be described by

$$F_{in} = 2 \int_0^\infty B_\nu(T_*)\, d\nu \int \sin\theta \cos\phi \, d\Omega \,, \tag{A.1}$$

where $d\Omega = \sin\theta \, d\theta \, d\phi$. The angle theta goes from 0 to θ_{max}, where θ_{max} can be described by $\arcsin(R_*/a)$ according to the geometries in Fig. A.1. The angle ϕ goes from 0 to $\pi/2$ according to Fig. A.2. However, this would only describe half the stellar disk, which is why (A.1) has a factor of 2 in front.

$$F_{in} = 2 \int_0^\infty B_\nu(T_*)\, d\nu \int_0^{\theta_{max}} \int_0^{\phi_{max}} \sin^2\theta \cos\phi \, d\phi \, d\theta \tag{A.2}$$

The first integral can be solved using Stefan-Boltzmann's law $\pi \int_0^\infty B_\nu(T_*) d\nu = \sigma T_*^4$ and after solving all integrals one gets the incoming flux in terms of the stellar temperature T_*,

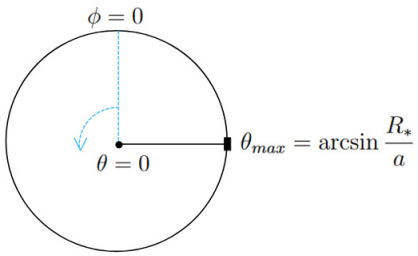

Figure A.2: The white dwarf viewed from the disk to visualize the minimum and maximum angles for θ and ϕ.

stellar radius R_*, and disk radius a.

$$F_{in} = \frac{\sigma T_*^4}{\pi} \left(\arcsin \frac{R_*}{a} - \frac{R_*}{a} \sqrt{1 - \left(\frac{R_*}{a} \right)^2} \right) \tag{A.3}$$

Using a third-order Taylor expansion for $x = 0$ with $x = \frac{R_*}{a}$ for a disk that is located relatively far away from the star ($R_* \ll a$), one gets the final equation for the incoming radiation

$$F_{in} = \frac{2}{3\pi} \left(\frac{R_*}{a} \right)^3 \sigma T_*^4 \,. \tag{A.4}$$

Appendix B

Plots

This section shows the behaviour of the Lambertian model for different inclinations, followed by the behaviour of the HG model for different disk radii.

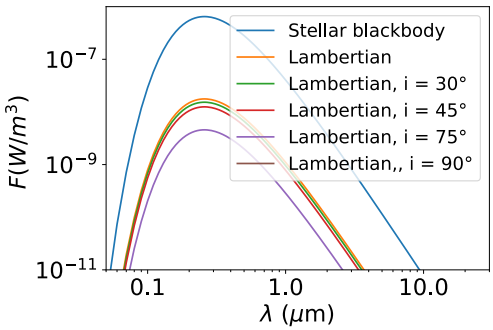

Figure B.1: The reflected flux density of white dwarf G 29-38 for different inclinations for a Lambertian surface. $i = 90°$ is invisible because no flux gets reflected to the observer when the disk is edge-on.

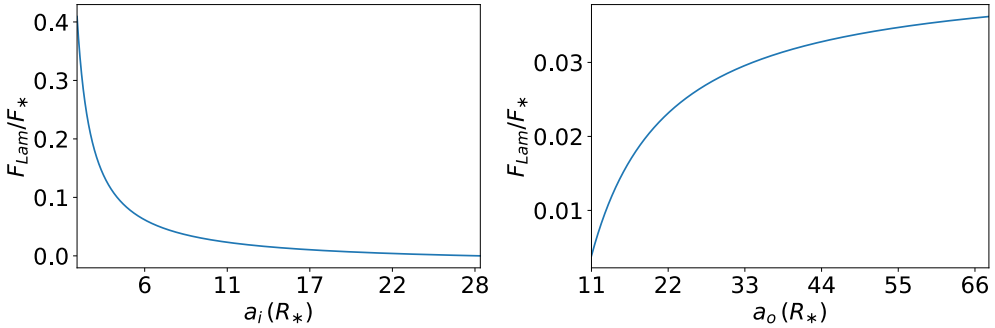

Figure B.2: Plot of the ratio between disk and stellar flux density for G 29-38 with varying inner (left) and outer radius (right). The disk is assumed to be face-on and the albedo and packing fraction are chosen to be 1.

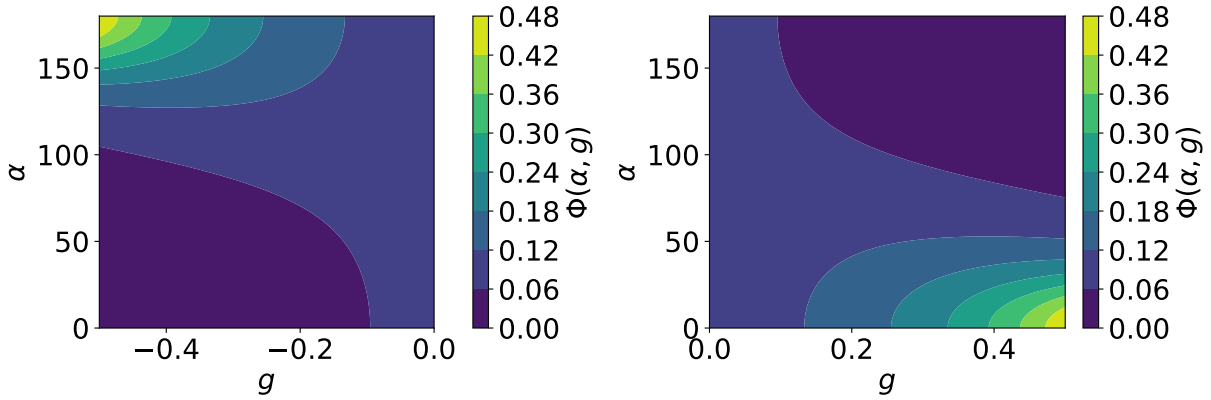

Figure B.3: Contour plot of the HG phase function as a function of α for varying g.

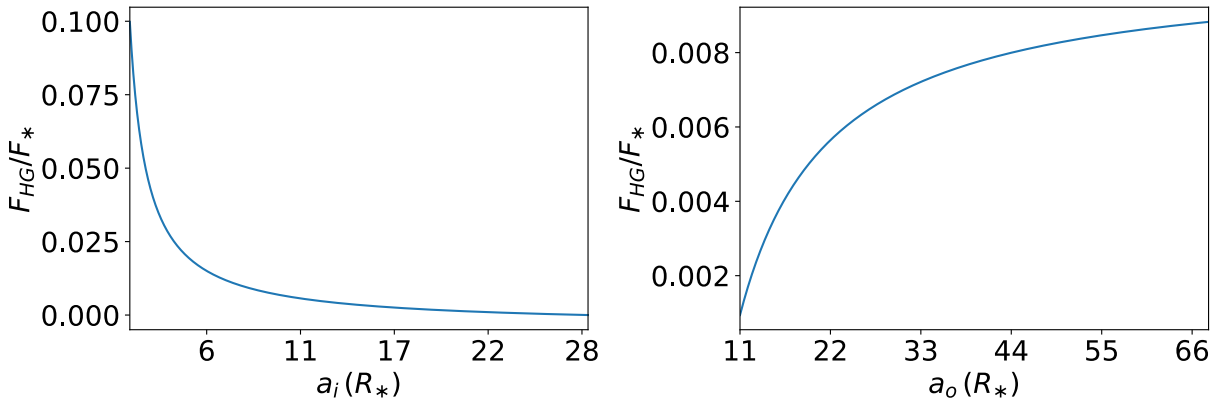

Figure B.4: Plot of the ratio between reflected and incoming flux for G 29-38 for varying inner (left) and outer radii (right). The inclination is set to zero and almost all radiation is assumed to be scattered isotropically $g = 0.1$.

Appendix C

Code

The code used for the plots can be viewed using the following link: `https://github.com/Amselii/Debris-Disk-Flux-Density.git`